GDCh

Research Articles

Angewandte
Chemie
International Edition
www.angewandte.org

Zeolites | Hot Paper |

Direct TEM Observation of Vacancy-Mediated Heteroatom Incorporation into a Zeolite Framework: Towards Microscopic Design of Zeolite Catalysts

Junyan Li, Alvaro Mayoral,* Yoshihiro Kubota, Satoshi Inagaki, Jihong Yu, and Osamu Terasaki*

Abstract: Incorporating hetero-metal-atom, e.g., titanium, into zeolite frameworks can enhance the catalytic activity and selectivity in oxidation reactions. However, the rational design of zeolites containing titanium at specific sites is difficult because the precise atomic structure during synthesis process remained unclear. Here, a titanosilicate with predictable titanium distribution was synthesized by mediating vacancies in a defective **MSE**-type zeolite precursor, based on a pre-designed synthetic route including modification of vacancies followed by titanium insertion, where electron microscopy (EM) plays a key role at each step resolving the atomic structure. Point defects including vacancies in the precursor and titanium incorporated into the vacancy-related positions have been directly observed. The results provide insights into the role of point defects in zeolites towards the rational synthesis of zeolites with desired microscopic arrangement of catalytically active sites.

Introduction

Zeolites are among the best materials for catalytic applications as aluminosilicate-type solid acid catalysts or as metallosilicate-type oxidation catalysts after introducing hetero-metal-atoms (HMAs) in the frameworks. Benefiting from the efficient steric restrictions caused by the regular and multi-dimensional pores systems of zeolites,[1] even a small amount of titanium (less than 2 wt %) incorporating into the zeolitic framework (titanosilicate) provides tremendous catalytic activity and selectivity for oxidation reactions such as propylene epoxidation or phenol hydroxylation with H_2O_2.[2] It is well-known that the first and greatest success of titanosilicate catalysts is TS-1 (titanium silicalite-1 with **MFI**-type framework) created by ENI (Ente Nazionale Idrocarburi).[3] The catalytic property and performance of metallosilicate could be fine-tuned by introducing HMAs to an optimized T atom (T = Si or Al) site in a pre-designed framework, taking the advantages of the diverse zeolite structures. However, the HMAs introduced in the framework prone to averagely distribute on all the T sites, showing no preference and the synthesis procedures usually experience uncontrollable metal substitution manners in the frameworks.[4]

On the other hand, zeolite catalysts are usually characterized by only exhibiting "shape-selectivity" based on a simple steric restriction inside pore as described above. As a general theory about catalysts, the activation energy of a catalytic reaction is lower than that of non-catalytic chemical reactions. Moreover, the activation energy of an enzymatic reaction is especially low. In the case of enzyme, there is a binding site that captures the substrate in the vicinity of an active site, bringing the substrate closer to the active site.[5]

[*] J. Li, Prof. J. Yu
State Key Laboratory of Inorganic Synthesis and Preparative Chemistry, College of Chemistry; International Center of Future Science, Jilin University
Changchun 130012 (China)

J. Li, Dr. A. Mayoral, Prof. O. Terasaki
Centre for High-resolution Electron Microscopy (ChEM), School of Physical Science and Technology, ShanghaiTech University
Shanghai 201210 (China)
and
Shanghai Key Laboratory of High-resolution Electron Microscopy, ShanghaiTech University
Shanghai 201210 (China)
E-mail: osamuterasaki@mac.com

Dr. A. Mayoral
Instituto de Nanociencia y Materiales de Aragón (INMA)
CSIC-Universidad de Zaragoza
50009 Zaragoza (Spain)

and
Laboratorio de Microscopias Avanzadas (LMA)
Universidad de Zaragoza
50180 Zaragoza (Spain)
E-mail: alvaro.mayoral@unizar.es

Prof. Y. Kubota, Dr. S. Inagaki
Division of Materials Science and Chemical Engineering
Yokohama National University
79-5 Tokiwadai, Hodogaya-ku, Yokohama 240-8501 (Japan)

This kind of cooperative action is a key factor for the amazing catalytic performance of enzymes. It would be epoch-making if we can introduce such substrate-binding site into zeolite framework and intentionally place it in a suitable positional relationship with the catalytically active site.

Silanol groups at silicon vacancies could function as the substrate-binding site inside the zeolite pores.[6] Some examples of well-defined silanols and ordered silicon vacancies are reported for SSZ-70 (*-**SVY**)[7] and SSZ-74 (-**SVR**),[8] respectively. These belong to a common category and one option of periodically locating binding sites and active sites. However, these are the interrupted framework structures as expressed in the framework type codes. For developing high performance catalysts, such frequent appearance of silanols is not really necessary from the viewpoint of structural stability and suitable hydrophilicity/hydrophobicity. In this sense, YNU-2 zeolites,[9] with **MSE**-type framework, are appropriate candidates as their precursor YNU-2P; it displays concentrated silicon vacancies with silanol groups at known T sites and these vacancies can be further modified to stabilize the framework by a post-synthesis procedure. In this work, learning from enzymes, we aimed at designing YNU-2-based titanosilicate catalyst and developing functions by locating both catalytically active titanium sites and silanol nests at specific positions of **MSE**-type framework that geometrically favor an organic substrate starting from pure-silica as-synthesized YNU-2P. By means of transmission electron microscopy (TEM), a comprehensive structural study making clear the role of vacancy at atomic scale from YNU-2P, via steamed YNU-2ST, to Ti-YNU-2 zeolites is presented.

Results and Discussion

A three-step point defect engineering (Figure 1a) was applied to synthesize Ti-YNU-2: (i) a pure silica pristine material with an organic structure-directing agent (OSDA) and highly concentrated structural vacancies in specific T sites, YNU-2P, was synthesized by dry-gel conversion; (ii) the framework was stabilized by a steaming process, in which the number and position of vacancies in the precursor were modified, leaving a few vacancies (YNU-2ST, ST= steaming); (iii) titanium atoms were preferentially grafted onto the prescribed structural vacancy sites in YNU-2ST using a vapor phase of $TiCl_4$ post treatment, forming Ti-YNU-2.[9] TEM analysis was performed to obtain direct structural evidence of the point defects including atomic site vacancies and the incorporation of the HMAs by combining electron diffraction (ED) in reciprocal (momentum) space for average information over a nanocrystal and scanning transmission electron microscopy (STEM) imaging for the local structural information at atomic resolution in the real space.

MSE-type zeolites have tetragonal space group $P4_2/mnm$ with unit cell parameters of $a = 18.25$ Å, $c = 20.56$ Å.[10] It contains a straight channel with 12-ring along [001] direction and two 10-ring channels along <110> and <100> directions with $4^6 5^8 6^6 10^4$ *mse*-2 cages forming by the intersecting channels (Figure S1). The projected structure (Figure 1b) along [001] incidence (plane group: *p4gm*) can be regarded as repeating the $4^2 5^2 6^2$ unit (one unit is marked by deeper color) by 4-fold rotation axis at the center of the 12-ring. Isolated single 4-ring (S4R) can be found at the 2-fold rotation axis (Figure 1b, Figure S2). Under this configuration, the S4Rs would be geometrically unstable due to the large T–O–T angles ($\approx 180°$). The eight distinct T sites in **MSE**-type framework superimpose to form four different atomic columns on the [001] projection, they are T1/T2, T3/T5, T4/T6 and T7/T8 columns (Figure S2). The three different YNU-2 type crystals with **MSE** topology, YNU-2P, YNU-2ST and Ti-YNU-2 are studied in the present work.

YNU-2P, pristine material. Based on previous reports, YNU-2P displays Si atomic vacancies, which have been investigated by X-ray diffraction obtaining the average structural information of the framework.[9a,b] Here, we turned into TEM to further investigate the structure of YNU-2P. Electron crystallography approach through selected area electron diffraction (SAED) patterns and three-dimensional electron diffraction (3D ED) were firstly conducted to detect if the number of vacancies was sufficient to be detected from a small volume in the range of (100–1000 nm)^3. The scattering power of the crystal would be altered by the existence of vacancies, as the structure factor would be affected. Simulated SAED patterns along the
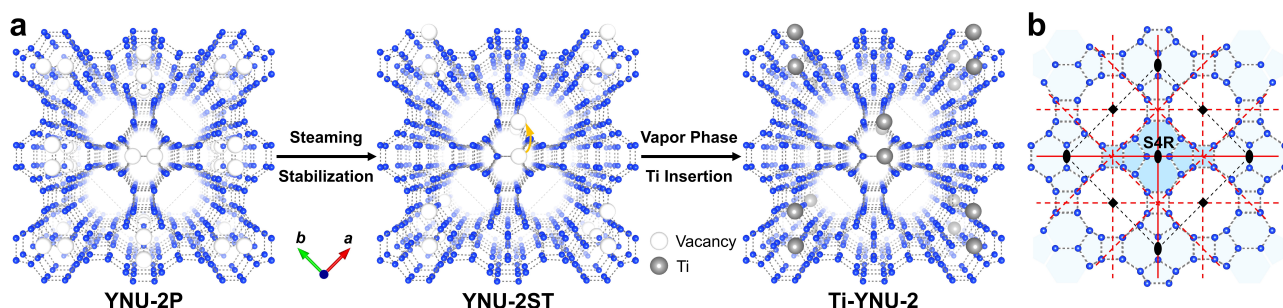
Figure 1. Synthetic route and structural models of YNU-2 zeolites. a) Designed procedure of incorporating titanium atoms into the **MSE**-type zeolite through point defect engineering. The **MSE**-type frameworks are viewed along [001] direction. b) Projected structural model of **MSE**-type framework along [001] direction. Symmetry symbols of 4-fold axis, 2-fold axis, mirror plane (red straight line) and glide plane (red dot line) are marked. For clarify the O bridges between the Si atoms are represented by dot lines and YNU-2P, the occluded OSDA is omitted for simplicity.

Angew. Chem. Int. Ed. **2022**, *61*, e202211196 (2 of 8)

© 2022 The Authors. Angewandte Chemie International Edition published by Wiley-VCH GmbH

[001] incidence of **MSE** and the corresponding scattering factors (Figure 2a, Figure S3) were calculated for **MSE**-type framework with different occupancies of the T7/T8 sites. The calculated structure amplitudes (Figure S4) and the diffraction intensities (Figure 2b) of the 200 reflection would decrease significantly while the 110 reflection would increase with the increase of the occupancy at T7/T8 sites. The relative intensity of the 200 over the 110 reflection was then used to determine the silicon vacancy in the crystals; Figure 2c corresponds to the calculated intensity relationship between the 200 and 110 reflections versus the occupancy at T7/T8 sites observing that the I(200)/(110) decreases as the sites being occupied. Experimental SAED patterns were recorded for the YNU-2P and the YNU-ST, see Figure 2d and 2e where it was evidenced the intensity difference between these two reflections. This estimation is in agreement with the experimental data obtained and the relative intensity is comparable to the theoretical value for the defective YNU-2P and the steamed YNU-2ST. However, this evaluation using only two reflections deviates from the actual value (Figure 2c) because the SAED patterns are affected by the diffraction condition and dynamical scattering, i.e., mistilting from the zone axis or the thickness of crystal. Therefore, 3D ED that collects diffraction data far from the zone axis and integrates all reflections over the three-dimensional reciprocal space would be suitable to determine the point defects in zeolites.[11]

In the 3D ED analysis, the structural vacancies in YNU-2P could be directly recognized in the ab initio structure solution that the T7 and T8 silicon as well as some connected oxygen atoms were missing. The electrostatic potential map in Figure 2f shows high potential level (yellow isosurface) of the nucleus and the electrons for all atoms except for the T7/T8 silicon and the surrounding oxygen atoms. Only a faint potential was observed at the T7/T8 sites and a weak potential for the oxygen connecting the T7/T8 and T3/T5 atoms (grey isosurface). After assigning the atoms to the corresponding peaks and refining the occupancies, the refinement converged (Table S1, Table S2 and Figure S5) into a model with chemical formula $Si_{96.1}O_{193.2}$ with a large amount of silicon vacancies at the S4Rs (T7/T8 sites).[12] Compared to the ideal **MSE**-type silica with chemical formula $Si_{112}O_{224}$, YNU-2P presented about 15.9 silicon vacancies per unit cell according to the 3D ED data. In addition, a residual potential attributed to the OSDA molecules, was clearly observed in the 12-ring straight channels and in the *mse*-2 cages (Figure 2g, Figure S6). Compared to the other characterization methods such as spectroscopy or nuclear magnetic resonance (NMR), ED can provide averaged structural information and number of vacancies in a similar manner as X-ray crystallography with the advantage of controlling the volume of analysis being as small as hundreds of nms, giving useful understandings to begin the defect analysis of any zeolite framework.
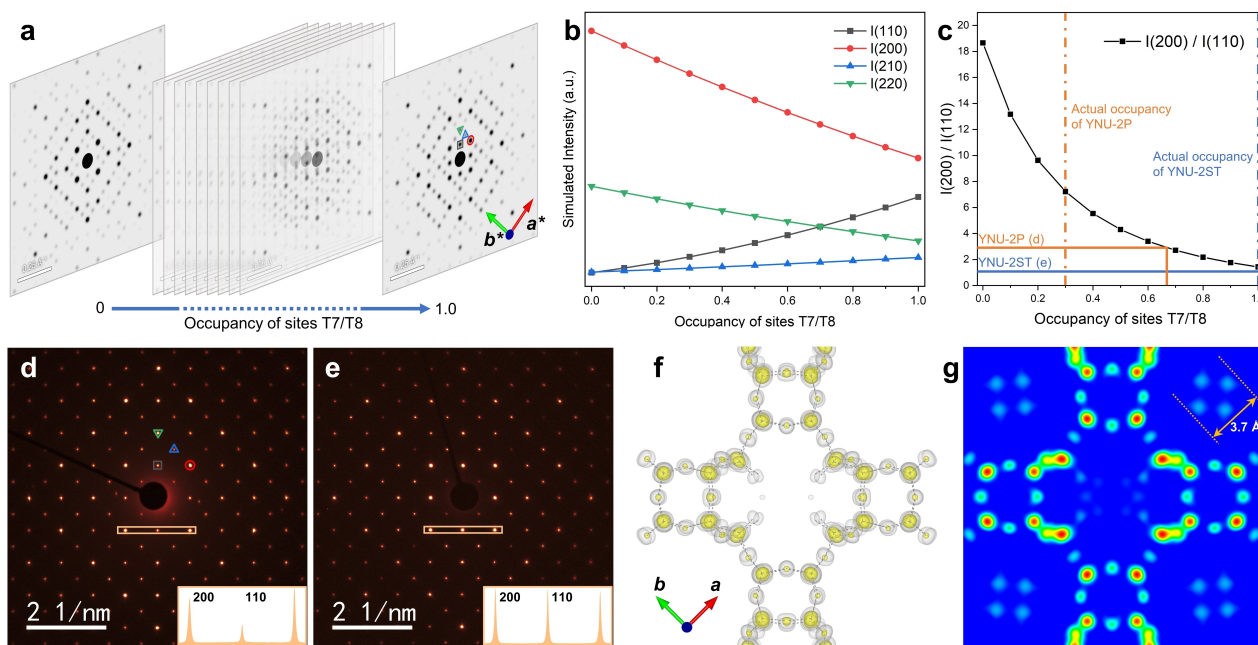
Figure 2. Electron diffraction study of YNU-2P. a) Simulated SAED patterns of the **MSE**-type framework with different T7/T8 site occupancies. b) Diffraction intensities for the selected reflections obtained from the SAED simulation. c) Diffraction intensity ratio between 200/110 reflections versus the site T7/T8 occupancy. The corresponding values obtained from YNU-2P (d) and YNU-2ST (e) experimental SAED patterns are marked by colored solid lines while the actual T7/T8 occupancy values from X-ray study are marked by the vertical dashed lines. d, e) Experimental SAED patterns of YNU-2P and YNU-2ST with the insets of intensity plots along a line containing the 200 and 110 reflections. f) Observed electrostatic potential map of YNU-2P from 3D ED data. The yellow and grey isosurface represent high and low level of potential, respectively. g) Projection of observed electrostatic potential color-map of YNU-2P along [001] direction, the high and low electrostatic potential value are shown by red and blue color, respectively.

Angew. Chem. Int. Ed. **2022**, *61*, e202211196 (3 of 8)

© 2022 The Authors. Angewandte Chemie International Edition published by Wiley-VCH GmbH

To retrieve direct local information, we turned into spherical aberration corrected (Cs-corrected) STEM to study the atomic structure of the YNU-2 materials. YNU-2P was found to be remarkably unstable in comparison with other zeolites, which resulted in a framework disruption after short beam exposure, forcing to work under very low dose conditions ($\approx 500\,e\,\text{Å}^{-2}$). Such a high instability could be directly related to the large number of vacancies present in the crystal. Under these experimental conditions, the signal-to-noise ratio (SNR) was relatively low when conventional detectors such as annular dark field (ADF) were used; therefore, a segmented annular all-field detector was employed to obtain the phase contrast images using a quantitative differential phase contrast (qDPC) method.[13] Figure 3a shows the high-resolution Cs-corrected STEM qDPC micrograph at the edge of an YNU-2P crystal taken along the [001] incidence. Despite the large number of defects, the Fourier diffractogram, shown inset, presents a four-fold axis and corroborating a very good crystallinity. A significant distinct feature in comparison with most of the zeolite images reported, it is the signal detected inside the pores; the 12-ring channel present a "rounded" signal of about 3.7 Å. By comparing this data with the structure solution obtained from 3D ED (Figure 2g), this signal was attributed to the direct visualization of the organic molecules from the OSDA within the zeolitic pores. A closer visualization (Figure 3b which is a magnified view of the white rectangle in Figure 3a) revealed an inhomogeneous distribution of the vacancies, S4Rs, along the framework pointed by coloured squares. Although analysis of the number of vacancies based on STEM imaging has not been reached to quantitative level yet, domains without and with partially and fully occupied silicon at T7/T8 sites can be clearly observed, marked by blue, orange, and yellow squares, respectively in Figures 3b and 3c. The intensity profiles across the S4Rs are shown together with the distance between neighbouring T7/T8 in Figure S7, where the intensity difference can be seen at these sites.

Overall, average crystallographic information and local distribution of the structural vacancies in YNU-2P were evaluated through ED and STEM imaging at atomic level. These results highlight that atomic-resolution real-space direct visualization is capable of revealing the existence of point defects as well as the location of the OSDA as demonstrated for YNU-2P. Furthermore, it indicates that this methodology can be extrapolated to other zeolites as YNU-2P has been found to be highly unstable, which is the main difficulty to analyse these materials.

YNU-2ST, steamed material. The substantial silicon vacancies make YNU-2P a suitable receiver (or acceptor) for silicon atoms or HMAs; however, the fragile framework would be destroyed during the high-temperature post treatment required to incorporate them. Subsequently, a steaming process[14] was conducted to stabilize YNU-2P followed by the calcination to remove the OSDA. According to the 3D ED analysis, almost all Si vacancies inside the YNU-2P were filled after steaming, forming YNU-2ST (Table S1). Low-magnification STEM ADF and secondary electron images (SEI) were collected to characterize the morphology of the YNU-2ST and to compare it with the parental material (Figure S8), revealing a significant contrast variation (dark spots) associated to the generation of intracrystalline mesopores.

The Cs-corrected STEM qDPC image, along [001] incidence of YNU-2ST, is shown in Figure 4a. A significant experimental difference observed between YNU-2P with YNU-2ST was the improved electron beam stability, also related to the thermal stability that is associated to the reduction of vacancies, which allowed working with higher electron dose ($\approx 2800\,e\,\text{Å}^{-2}$). Figure 4a depicts a fully formed **MSE**-type framework where all the T atoms can be identified. However, thickness-mass contrast is suppressed in a qDPC image dominated by phase contrast, especially after the high pass filtering for qDPC images (Figure S9). Low angle ADF (LAADF) imaging also allows working under low-dose conditions to minimize electron beam damage while maintaining the thickness-mass contrast. Significant contrast variations, which are attributed to thickness variations across the specimen, could be observed in the Cs-corrected STEM LAADF micrograph (Figure 4b).
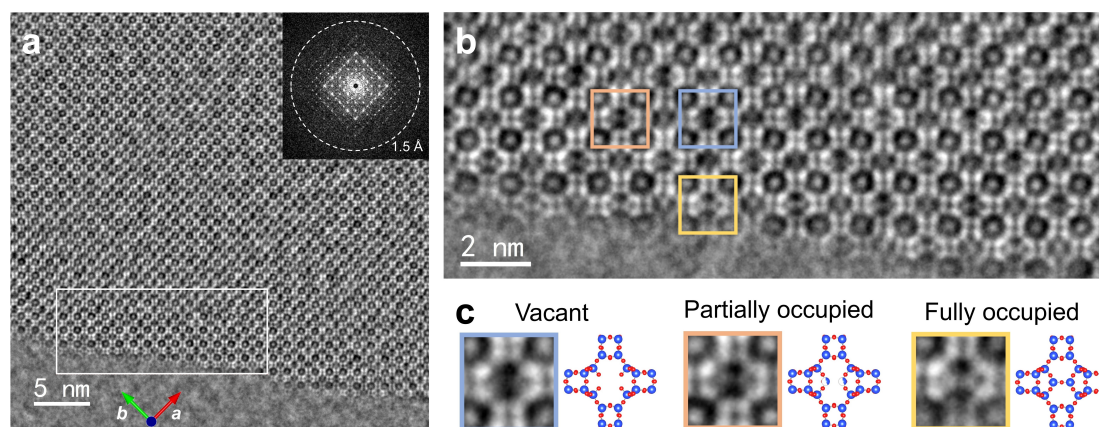
Figure 3. Local visualization of structural vacancies in YNU-2P. a) Cs-corrected STEM qDPC image of YNU-2P along [001] incidence with the inset of Fourier diffractogram. b) Enlarged image of the white rectangle in (a). c) Regions of interest with different amounts of vacancies on the S4Rs.
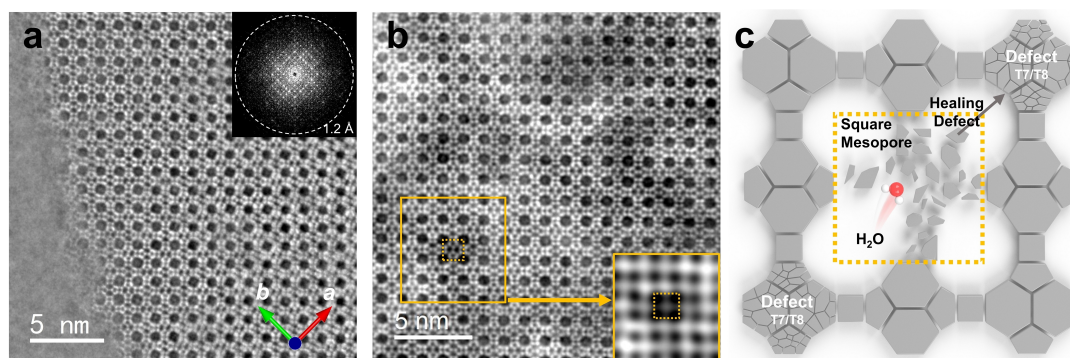
Figure 4. STEM imaging of YNU-2ST. a) Cs-corrected STEM qDPC image of YNU-2ST along [001] incidence with the inset of Fourier diffractogram. b) Cs-corrected STEM LAADF image of YNU-2ST along [001] incidence. The inset corresponds to the low pass filtered image of the region highlighted by a golden solid square for better mesopore morphology visualization. c) A schematic diagram of the mesopore formation and defect healing during the steaming process in YNU-2 zeolite. The golden dash square represents the mesopore.

Both types of imagining modes corroborate the successful healing of the framework, where all (or at least most of them) S4Rs are present. The golden square in Figure 4b corresponds to one of these low contrast regions, while the dashed square indicates the T7/T8 site, the S4Rs, where the concentrated vacancies in YNU-2P were observed. To facilitate the visualization of the mesopores formed (low contrast), Figure 4b was low pass filtered, to exclude the high-frequency information (that corresponds to the fine structure of the **MSE**-type framework), where the mesopore marked by a dashed rectangle is identifiable. Based on this image, a schematic model was created, Figure 4c. Combining the atomic-scale information obtained from YNU-2P and YNU-2ST (vacancies, healing and mesopore formation), it is safe to assume that the mesopore generation begins at a highly defective S4R region, i.e., vacancies at T7/T8 site. Hence, this square shaped dark contrast observed in the Cs-corrected STEM LAADF image would indicate where defective S4Rs (T7/T8) was present in YNU-2P, while larger mesopores were formed due to the existence of regions with large-area agglomerated vacancies. The nitrogen adsorption-desorption measurement of the calcined YNU-2ST at 77 K is a type I(b) isotherm as shown in Figure S10.[15] This type of the isotherm indicates the existence of mesopores formed during the steaming treatment as well as the intrinsic micropores of the **MSE**-type framework. This result is consistent with the STEM observation of YNU-2ST.

It has been widely assumed that the mesopores generated in the zeolites by post treatment experiments are closely related to structural defects such as vacancies, aluminum atoms or HMAs.[16] In principle, it would be possible to control the morphology of the mesopore produced by post treatment experiments, starting from a zeolite crystal with a known defective position. In the present scenario, defect sites, especially S4Rs with more than one vacancy, are unstable under the chemical attack of water molecules. The silanol groups near the defect sites together with the adjacent silicon would be leached out, resulting in the degradation of the framework forming a mesopore, creating the smallest square mesopore as illustrated in Figure 4c. The $Si(OH)_4$ species leached would heal the other isolated vacancies after migration through channels. The H_2O adsorption-desorption measurement of the calcined YNU-2ST at 298 K provided a type V isotherm as shown in Figure S10b, indicating that H_2O clusters are formed in the local hydrophilic space within the hydrophobic micropores prior to micropore-filling.[17] This suggests that that some silanol groups may be aggregated in the micropores in the calcined YNU-2ST. Finally, YNU-2ST increased its stability due to the significant reduction of the point defects. Indeed, YNU-2ST crystals can endure more than five times of electrons under STEM imaging condition (2800 vs 500 $e\,\text{Å}^{-2}$), converting YNU-2ST in a zeolite similar, in terms of ebeam stability, to other frameworks commonly studied by electron microscopy such as **MFI** or **FAU**. Further imaging was performed along the [110] and [100] incidence of the **MSE**-type framework (Figure S11) confirming the completeness of the framework. The reconstructed model and the cross sections from the electron tomography of YNU-2ST crystal (Figure S12) show that the mesopores are located inside of the crystal, which coincides with our STEM observations that vacancies were mostly distributed inside the crystals in the parental YNU-2P (Figure 3).

Ti-YNU-2. In the final step, titanium atoms were incorporated into the zeolite framework through a gas phase (under $TiCl_4$/Ar gas flow) insertion process into YNU-2ST. The T-sites occupied by HMAs, which are the interruption of the TO_4 framework, can be regarded as point defects although such sites are catalytic active sites and do not cause framework instability. Despite there are several reports using STEM for imaging various zeolite frameworks, obtaining data to quantitatively analyze the location and number of HAMs in the structures is still complicated.[18] The signal produced by HMAs that do not present any periodicity would be buried under the strong signal of periodic frameworks. Therefore, the preparation of a very thin specimen is crucial to enhance the elemental contrast while controlling the electron dose in order to image HMAs in the framework.[19] Here, the atomic resolution Cs-corrected STEM LAADF imaging of Ti-YNU-2 has been performed over a sample prepared by ultramicrotomy. Cs-corrected STEM LAADF of Ti-YNU-2 along [001] incidence proc-

essed by different methods together with the qDPC images are shown in Figure S13 and Figure 5. By either image denoising or averaging, not only all the T atoms but also the oxygen atoms are distinguishable.

The LAADF image of Ti-YNU-2 along [001] incidence with distinct signal that might come from titanium atoms is exhibited in Figure 5a in which the T7/T8 atoms (pointed out by golden arrow) in the center of the blue rectangle appears to be brighter than the rest of its neighbors (where thickness should be the same). Image contrast analysis becomes more complicated in the area denoted with an orange rectangle because the overall intensity increases from the bottom left to the top right due to the thickness variation across the crystal. Nevertheless, it is still possible to recognize a brighter contrast rising on two sites corresponding to T7/T8 and into a less extent T1/T2 (pointed out by green arrow), see the intensity distributions shown by surface plots in Figure S14. STEM image simulations (Figure 5b) were carried out to interpret the observed contrast, observing a similar contrast variation when 1/4 of the silicon atoms at specific columns was substituted by titanium (equal to 1/112 of the framework silicon atoms). The simulated results show that the incorpo-

ration of the titanium atoms brings a distinguishable contrast difference, and it is reasonable to assign the above-mentioned bright contrast to titanium atoms. Compared to high angle ADF (HAADF) or middle angle ADF (MAADF), the LAADF data would provide weaker elemental contrast and could be affected by phase contrast into some extent. STEM-ADF image simulations were carried out using different collecting angles demonstrating that the titanium is potentially observable in the LAADF image. However, for MAADF due to the high level of noise of the images, such contrast was not so clearly evidenced (Figure S15). In addition, the intensity fluctuations that could appear in the image owed to the high noise in the low dose analysis was also evaluated by simulating the image with a similar dose (similar noise) to the experimental one proving that under these conditions the titanium signal is detectable (Figure S16). According to the inductively coupled plasma atomic emission spectroscopy (ICP-AES) analysis, the silicon to titanium ratio in Ti-YNU-2 equals to 91, equivalent to 1.2 titanium atoms per unit cell. The existence of titanium in Ti-YNU-2 locally was confirmed by electron energy loss spectroscopy (EELS) analysis from the same crystal with rather low Ti-content where we performed
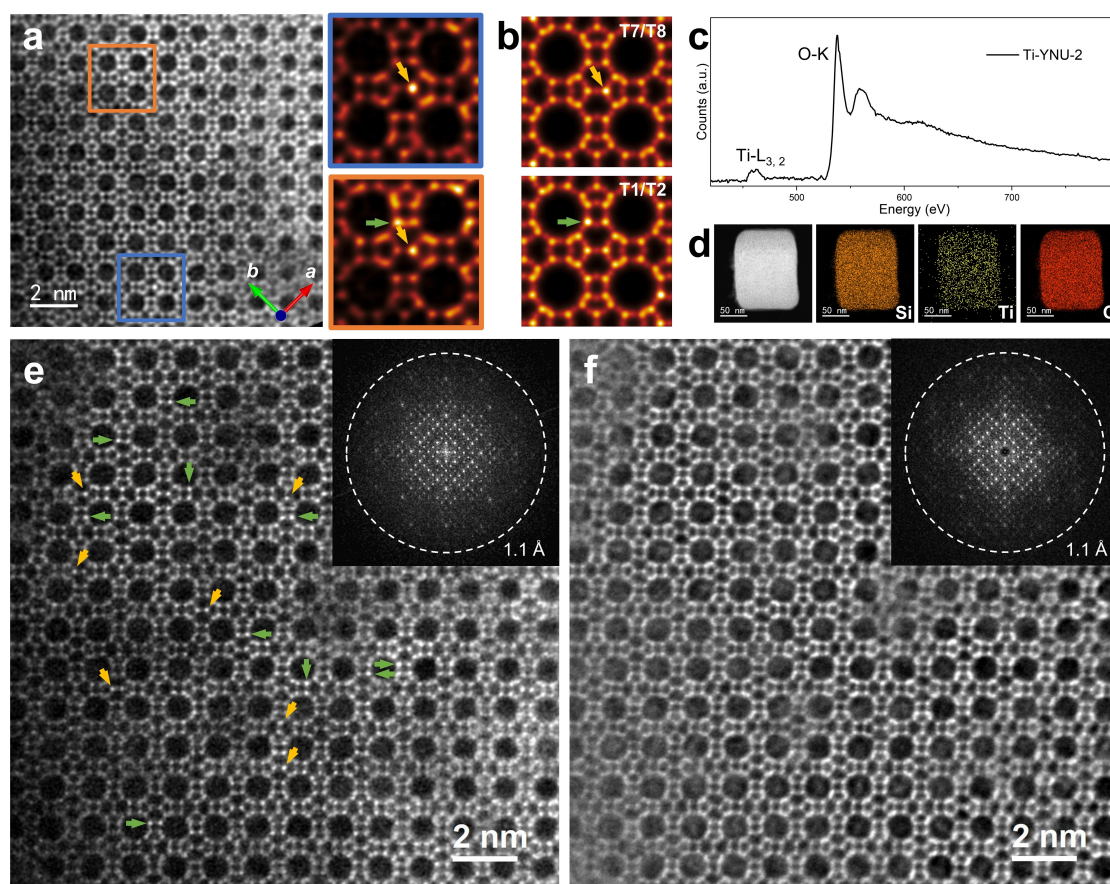
Figure 5. Probable positions of titanium in Ti-YNU-2. a) Cs-corrected STEM LAADF image along [001] incidence of Ti-YNU-2, two regions with distinct contrast differences are marked by colored rectangles and enlarged on the right. The T7/T8 and T1/T2 sites assigned to titanium atoms have been pointed out by golden and green arrows, respectively. b) Simulated images of Ti-substituted **MSE** on T7/T8 sites and T1/T2 sites, equivalent to one titanium atom per unit cell. c) EELS spectrum of Ti-YNU-2. d) EDS elemental mapping of Ti-YNU-2. e, f) Cs-corrected STEM LAADF and qDPC images of Ti-YNU-2 along [001] incidence with large field of view.

detailed image analysis at atomic scale, Figure 5c. The Ti-$L_{3,2}$ edges due to the presence of titanium in the framework as well as the O-K edge due to the zeolitic framework are clearly identified. Energy dispersive spectroscopy (EDS) and EELS elemental mapping indicate a uniform distribution of titanium along the entire crystal (Figure 5d, Figure S17 and Figure S18). Therefore, titanium atoms can be discussed at those positions with distinctly brighter contrast than the closest atoms in the LAADF data since no extra contrast corresponding to extra-framework titanium species has been found on the surface of crystals or in the channels (Figure S19). Based on these observations, the titanium atoms would be mostly located at the T7/T8 and T1/T2 sites of the **MSE** framework (Figure 5e). It is worth noticing that such contrast variations are not apparent in the qDPC data of the Ti-YNU-2 (Figure 5f).

Although point vacancies were not observed (as those observed in YNU-2P) in YNU-2ST, the fact that titanium atoms went into the T7/T8 sites suggests that some point vacancies remained which were undetectable through electron microscopy. Previous NMR study suggested a small amount of vacancies remained which are undetectable by X-ray crystallography.[9b] We speculated that the remaining T7/T8 structural vacancies in YNU-2ST are the adaptors for the titanium atoms during the vapor reaction. The presence of titanium atoms at T1/T2 sites can be explained by the silicon migration hypothesis proposed by Ikeda et al.[9b] that silicon may migrate from T7/T8 to T1/T2 via their adjacent T3/T5 sites during the structure rearrangement under steaming process. A recent work by Petkov et al. suggested that among the eight T sites in **MSE**, the most energetically favorable configuration would be titanium at T1 position, followed by T6, T2 and T4.[20] According to this, some of the titanium atoms would migrate to the most energetically favorable T1/T2 sites during the titanium incorporation as it was observed by STEM imaging. The titanium atoms located at T1/T2 sites provide active reaction centers facing the 12-rings of Ti-YNU-2, which gives a direct explanation to the superior catalytic activity and selectivity of Ti-YNU-2 in the hydroxylation reaction of phenol, forming *para*-isomer, hydroquinone (HQ).[9c] Kubota and co-workers proposed a possible picture of a defined transition state, involving the interaction between a Ti-complex moiety and an organic substrate trapped inside the micropores with the aid of some hydrogen bonds like "entropy trap" common in enzyme catalysis. Based on the observations reported here, the better picture of the defined transition state could be modified as shown in Figure S20. The originally proposed concept is still valid while the determination of the titanium atom siting is only achieved in this work.

Conclusion

In conclusion, the present work represents a comprehensive study on the analysis of point defects in **MSE**-type framework (YNU-2 zeolites) by atomically resolved electron microscopy (combining imaging and diffraction with spectroscopy). These results show how it would be possible to obtain titanium-substituted YNU-2 with a pre-designed titanium distribution. The point defects including silicon vacancies and substituted titanium atoms have been carefully studied combining the electron crystallography and advance Cs-corrected STEM. For the first time, these two kinds of structural defects have been directly imaged. Furthermore, the formation of mesopores during the steaming process and the modification of the point defects have been elucidated. Although it is still necessary to fully control in the incorporation of HMAs to specific position with cooperative relationship to subtract-binding site, these results highlight the importance of low-dose Cs-corrected STEM imaging providing direct atomic level information of point defects and HMA incorporation that will assist the rational design of new zeolites with selected properties by manipulating the point defects in the framework.

We believe that this type of analysis can be extended to other zeolites, especially considering the instability that YNU-2P presented in comparison with other frameworks. This is also the case for the metal identification, where Ti would be more complicated than noble metals (highly used in catalysis) due to its lower atomic number. However, this latest aspect requires a case-by-case evaluation as sample preparation, amount and location of the metals and any aspect that could affect the experimental data acquisition will strongly affect the analysis. Nevertheless, the results presented here clearly evidenced that local analysis of zeolites at atomic level can be achieved allowing the discussion of single atom active sites and single atomic catalysis.

Conflict of Interest

The authors declare no conflict of interest.

Data Availability Statement

The data that support the findings of this study are available on request from the corresponding author. The data are not publicly available due to privacy or ethical restrictions.

[1] S. M. Csicsery, *Pure Appl. Chem.* **1986**, *58*, 841–856.

[2] a) D. R. C. Huybrechts, L. D. Bruycker, P. A. Jacobs, *Nature* **1990**, *345*, 240–242; b) M. G. Clerici, P. Ingallina, *J. Catal.* **1993**, *140*, 71–83; c) B. Notari, *Stud. Surf. Sci. Catal.* **1988**, *37*, 413–425.

[3] M. Taramasso, G. Perego, B. Notari, US Patent 4410501, **1983**.

[4] a) C. Lamberti, S. Bordiga, A. Zecchina, G. Artioli, G. Marra, G. Spanò, *J. Am. Chem. Soc.* **2001**, *123*, 2204–2212; b) W. Fan, R.-G. Duan, T. Yokoi, P. Wu, Y. Kubota, T. Tatsumi, *J. Am. Chem. Soc.* **2008**, *130*, 10150–10164; c) B. Tang, W. Dai, X. Sun, N. Guan, L. Li, M. Hunger, *Green Chem.* **2014**, *16*, 2281–2291.

[5] a) A. Sievers, M. Beringer, V. Rodnina Marina, R. Wolfenden, *Proc. Natl. Acad. Sci. USA* **2004**, *101*, 7897–7901; b) J.-K. Lee, M. C. Kung, H. H. Kung, *Top. Catal.* **2008**, *49*, 136–144.

[6] N. Rai, S. Caratzoulas, D. G. Vlachos, *ACS Catal.* **2013**, *3*, 2294–2298.

[7] S. Smeets, Z. J. Berkson, D. Xie, S. I. Zones, W. Wan, X. Zou, M. F. Hsieh, B. F. Chmelka, L. B. McCusker, C. Baerlocher, *J. Am. Chem. Soc.* **2017**, *139*, 16803–16812.

[8] C. Baerlocher, D. Xie, L. B. McCusker, S.-J. Hwang, I. Y. Chan, K. Ong, A. W. Burton, S. I. Zones, *Nat. Mater.* **2008**, *7*, 631–635.

[9] a) Y. Koyama, T. Ikeda, T. Tatsumi, Y. Kubota, *Angew. Chem. Int. Ed.* **2008**, *47*, 1042–1046; *Angew. Chem.* **2008**, *120*, 1058–1062; b) T. Ikeda, S. Inagaki, T. Hanaoka, Y. Kubota, *J. Phys. Chem. C* **2010**, *114*, 19641–19648; c) M. Sasaki, Y. Sato, Y. Tsuboi, S. Inagaki, Y. Kubota, *ACS Catal.* **2014**, *4*, 2653–2657.

[10] D. L. Dorset, S. C. Weston, S. S. Dhingra, *J. Phys. Chem. B* **2006**, *110*, 2045–2050.

[11] M. Gemmi, E. Mugnaioli, T. E. Gorelik, U. Kolb, L. Palatinus, P. Boullay, S. Hovmoller, J. P. Abrahams, *ACS Cent. Sci.* **2019**, *5*, 1315–1329.

[12] Deposition Numbers 2175076 (for YNU-2P), 2175070 (for YNU-2ST) and 2175063 (for Ti-YNU-2) contain the supplementary crystallographic data for this paper. These data are provided free of charge by the joint Cambridge Crystallographic Data Centre and Fachinformationszentrum Karlsruhe Access Structures service.

[13] a) N. Shibata, S. D. Findlay, Y. Kohno, H. Sawada, Y. Kondo, Y. Ikuhara, *Nat. Phys.* **2012**, *8*, 611–615; b) A. Ishizuka, M. Oka, T. Seki, N. Shibata, K. Ishizuka, *Microscopy* **2017**, *66*, 397–405; c) L. Liu, N. Wang, C. Zhu, X. Liu, Y. Zhu, P. Guo, L. Alfilfil, X. Dong, D. Zhang, Y. Han, *Angew. Chem. Int. Ed.* **2020**, *59*, 819–825; *Angew. Chem.* **2020**, *132*, 829–835; d) B. Shen, X. Chen, X. Fan, H. Xiong, H. Wang, W. Qian, Y. Wang, F. Wei, *Nat. Commun.* **2021**, *12*, 2212.

[14] a) J. Klinowski, J. M. Thomas, C. A. Fyfe, G. C. Gobbi, *Nature* **1982**, *296*, 533–536; b) K. Iyoki, K. Kikumasa, T. Onishi, Y. Yonezawa, A. Chokkalingam, Y. Yanaba, T. Matsumoto, R. Osuga, S. P. Elangovan, J. N. Kondo, A. Endo, T. Okubo, T. Wakihara, *J. Am. Chem. Soc.* **2020**, *142*, 3931–3938.

[15] M. Thommes, K. Kaneko, A. V. Neimark, J. P. Olivier, F. Rodriguez-Reinoso, J. Rouquerol, K. S. W. Sing, *Pure Appl. Chem.* **2015**, *87*, 1051–1069.

[16] a) I. C. Medeiros-Costa, E. Dib, N. Nesterenko, J.-P. Dath, J.-P. Gilson, S. Mintova, *Chem. Soc. Rev.* **2021**, *50*, 11156–11179; b) L. Zhang, K. Chen, B. Chen, J. L. White, D. E. Resasco, *J. Am. Chem. Soc.* **2015**, *137*, 11810–11819.

[17] O. Talu, F. Meunier, *AIChE J.* **1996**, *42*, 809–819.

[18] a) A. Mayoral, T. Carey, P. A. Anderson, A. Lubk, I. Diaz, *Angew. Chem. Int. Ed.* **2011**, *50*, 11230–11233; *Angew. Chem.* **2011**, *123*, 11426–11429; b) A. Mayoral, Q. Zhang, Y. Zhou, P. Chen, Y. Ma, T. Monji, P. Losch, W. Schmidt, F. Schüth, H. Hirao, J. Yu, O. Terasaki, *Angew. Chem. Int. Ed.* **2020**, *59*, 19510–19517; *Angew. Chem.* **2020**, *132*, 19678–19685; c) A. Mayoral, J. Coronas, C. Casado, C. Tellez, I. Díaz, *ChemCatChem* **2013**, *5*, 2595–2598; d) C. Li, Q. Zhang, A. Mayoral, *ChemCatChem* **2020**, *12*, 1248–1269; e) Y. Zhang, D. Smith, J. E. Readman, A. Mayoral, *J. Phys. Chem. C* **2021**, *125*, 6461–6470.

[19] A. E. Watts, M. M. Lozinska, A. M. Z. Slawin, A. Mayoral, D. M. Dawson, S. E. Ashbrook, B. E. Bode, A. I. Dugulan, M. D. Shannon, P. A. Cox, A. Turrina, P. A. Wright, *Angew. Chem. Int. Ed.* **2020**, *59*, 15186–15190; *Angew. Chem.* **2020**, *132*, 15298–15302.

[20] P. S. Petkov, K. Simeonova, I. Z. Koleva, H. A. Aleksandrov, Y. Kubota, S. Inagaki, V. Valtchev, G. N. Vayssilov, *Molecules* **2021**, *26*, 7296.